Giant coercive-field (Hc @ 2K > 17 T) by freezing of magnetic domains in BaFe_2(PO_4)_2

Olivier Mentré, Claire Minaud, Jonas Wolber, Victor Duffort, Alain Pautrat, Vassily-S. Stolyarov, Angel-M. Arevalo-Lopez

Giant Coercive-Field ($H_{c\ @\ 2\ K}$ > 17 T) by freezing of magnetic Domains in $BaFe_2(PO_4)_2$

Olivier Mentré[1, *], Claire Minaud[2], Jonas Wolber[1,3], Victor Duffort[1], Alain Pautrat[4], Vassily-S. Stolyarov[5], Angel-M. Arevalo-Lopez[1]

[1]UCCS – Axe Chimie du Solide, UMR-CNRS 8181, Ecole centrale/Université de Lille, France

[2]Univ. Lille, CNRS, INRAE, Centrale Lille, Univ. Artois, FR 2638 - IMEC - Institut Michel-Eugène Chevreul, F-59000, Lille, France

[3] ILL Institut Max von Laue - Paul Langevin, 71, avenue des Martyrs , Grenoble cedex , France

[4]CRISMAT, CNRS, Normandie Univ, ENSICAEN, UNICAEN, France

[5]Advanced Mesoscience and Nanotechnology Centre, Moscow Institute of Physics and Technology, Russia

* E-mail: olivier.mentre@univ-lille.fr

Abstract:

In the 2D-Ising $BaFe_2(PO_4)_2$ ferromagnet (FM), the competition between giant magneto-crystalline anisotropy and strong FM couplings creates remarkably narrow magnetic domain walls. These domains freeze below $T_F \approx 15$ K which is accompanied by progressive "*soft-magnet*" → "*super-hard magnet*" transition at both sides of T_F. In the hard-regime, the coercive force is above 17 T at 2 K. At 5K, we calculate a $B.H_{max}$ figure of merit (*i.e.*, energy product) of 6.5 MG.Oe superior to what observed in most permanent magnet oxides. This allows for the printing above T_F and robust locking below T_F of any magnetization between the saturation limits. The outstanding H_c value surpasses the standards by far, and questions about the unusually strong pinning effects. They plausibly stem from intrinsic effects due to the abrupt spin reversal across the narrow domain walls, estimated to ~16 Å thick. Besides the observation of the domain wall structure by magnetic-force microscopy in various conditions, our specific heat shows their thermodynamic signature down to the freezing temperature.

1. Introduction

The magnetic domain walls are the microstructural elements connecting the microscopic and macroscopic properties of magnets and their origin is found in the combination of most of the ingredients of magnetism: crystal-structure, magneto-crystalline anisotropy, magnetic exchange, dipolar interactions, and crystal defects [1]. Their interfacial domain walls (DWs) which separate spins rotated by 180° in uniaxial magnets have demonstrated unexpected technological interests, such as their propagation under spin polarized current able to

exceptional capabilities for bit carriers in racetrack memories, data transfer, and spintronic devices [2–4]. In a simplified view, the width of the domain walls results from the competition between two opposing energies: i) the magneto-crystalline anisotropy energy which tend to align the spins in an antiparallel colinear way (narrow DWs) and ii) the exchange energy which tends to tilt two next spins by small angle values, leading to the common Bloch walls picture. Both of them find a compromise into the most favorable energetic state. It follows in highly anisotropic magnets, that the energy of narrow walls can be smaller than that of Bloch walls, such that narrow walls are frozen as long as the applied field is smaller than a critical field approximately equal to the coercive field. The coexistence of a large remanent magnetization and a large coercive field associated with this rare type of domain wall suggests that such materials may be pertinent permanent magnets, as first suggested in the early report of anomalous behavior by freezing of DWs in Dy_8Al_{12} and $TbNi_{1-x}Cu_x$, ($0<x<0.4$). The coercive force (H_c), defined as the external magnetic field able to demagnetize a sample, is the main parameter characterizing hard magnetic materials. It emerges from the pinning of the domains by lattice defects and quantifies the DWs energy and robustness [5]. For Dy_8Al_{12}, H_c = 2.1 T at 4.2 K, while the DW freezing temperature, T_F = 20 K. Although other examples about similar freezing phenomena have been occasionally reported, including on oxides such as Fe_3O_4 nanorods (with minor hysteretic magnetization effects) [6], and two-dimensional (2D) multiferroic $LuFe_2O_4$ (with giant coercivity $H_c \approx$ 9 T) [7], this phenomenology remains a curiosity. We recently evidenced the progressive passage from a "soft" to a so-called "super-hard" magnet by freezing of DWs in the 2D-Ising FM $BaFe_2(PO_4)_2$ on cooling below $T_F \sim$ 15 K. In this compound the Ising uniaxial magnetism was confirmed in early reports by extraction of the three critical exponents γ, β, δ from AC-susceptibility data, in fair agreement with their theoretical values [8]. The responsible enormous magnetic anisotropy results from accidentally degenerate (1*a*) and (2*e*) sub-levels of the t_{2g} manifold the $Fe^{2+}O_6$ (d^6, S = 2) octahedra of the honeycomb magnetic sub-units. This configuration with unevenly occupied degenerate levels is mandatory for Ising-like uniaxial magnetism. In our early-work, we have evidenced the robust labyrinthic magnetic domain structure under an applied field, and quantified the anisotropy which is predominant over the exchange interaction. In this work, we focus on the robust giant-coercivity extrapolated to >19 T at 0 K. Although it is unfair to compare such record-values with those of magnets generally reported at 300 K, we note superior behavior compared to what ideally predicted for the most common permanent magnets [9]. These values and the large $(BH)_{max}$ energy product figure of merit discussed later are relevant, due to the possibility to exploit very contrasted soft *vs.* super-hard magnetizations, just by changing the temperature ΔT = 10 K, which allows for the imprinting and freezing of multiple sample moments in a robust manner. Other data such as $C_p(T)$ are discussed.

2. $BaFe_2(PO_4)_2$ (BFPO): a mini-review

BFPO is isomorphic with other $BaM_2(XO_4)_2$ compounds (M^{2+} = Co, Ni; X^{5+} = P, V, As) [10], built on 2D-honeycomb layers magnetically and structurally disconnected ($d_{\text{inter-layer}} \approx$ 8-9 Å) by XO_4^{3-} groups and Ba^{2+} layers, Figure 1a. In contrast to other compounds of its family (quasi 2D-Heisenberg or -XY AFMs), it is a unique case of 2D Ising ferromagnet-oxide, T_C = 70 K, with a soft magnet behavior [8,10]. This situation is unique as sometimes met in isolated monolayer units only obtained after exfoliation see for instance CrI_3 [11]. This results in the exception of the *Mermin-Wagner* theorem, which fascinating signatures are: at T_C, all layers individually but collectively order FM with spins perpendicular to the layers, without significant inter-layer interactions. The typical in-plane and out-of-plane thermal magnetization are plotted in Figure 1b. The strong magneto-crystalline anisotropy is expected to be thickness-independent (thin film, nanodomains, crystallites, single crystals). The spin degrees of freedom

are only "↑" or "↓", not in-plane. It returns very specific 2D-magnetization S-like plots with strong remanent moment (> 7μ_B/FU) and weak coercive fields (*ca.* 50 Oe) acting as an easy spin-reversible material (soft magnet). The magnetocrystalline anisotropy can be estimated by the projected cross point of $M_{\parallel}(H)$ and $M_{\perp}(H)$ magnetization plots on oriented single crystals (the anisotropy constant K = 19 J. cm^{-3}) and by simulation of the inelastic neutron scattering spectra (9.3·J. cm^{-3} close to the highest reported-values of ~88· J. cm^{-3} for UCoGa [12]).
BFPO displays a unique re-entrant transition [13] due to spin-lattice interaction versus temperature: *R*-3 (paramagn.)$_{140K}$ → *P*-1 (paramagn.)$_{70K}$ → *R*-3 (ferromagn.). The corresponding anomalies detected on $\chi^{-1}(T)$ curves are shown in the Figure1c. It occurs due to the competition between the Ising FM that requires the *R*-3 symmetry and triclinic *Jahn-Teller* distortion due to the Fe^{2+} degenerate crystal field. Here the triclinic symmetry, blocks the establishment of the FM state at higher temperature [13,14].
Around 300°C, the sizeable creation of Fe-defects is perfectly controlled, activated by the Fe^{2+}/Fe^{3+} *redox couple*. BFPO releases up to 1/3rd of the original Fe content by exsolution according to the reaction [14]: $BaFe^{2+}_2(PO_4)_2 + 3x/2\ O_2 \rightarrow BaFe^{2+/3+}_{2-x}(PO_4)_2 + x/2\ Fe^{3+}_2O_3$. The reaction is reversible under dilute H_2 (even on single crystals!), as the BFPO crystal structure self-adapts to all ratios of Fe vacancies with flexible ordering [15]. We are also able to prepare Fe/Co and Fe/Ni complete solid solutions[16] which allows to tune the FM properties in Fe-rich regions. Our preliminary measurements validate also the freezing of domains in the Fe-rich members.

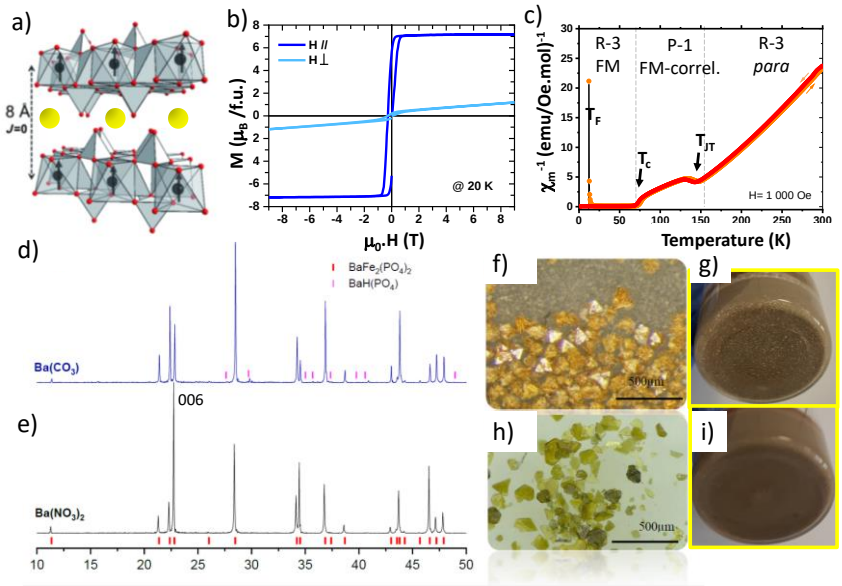

Figure 1: a) Layered crystal structure of $BaFe_2(PO_4)_2$ (Ba^{2+} in yellow; $Fe^{2+}O_6$ and PO_4 in grey). b) Anisotropic M(H) magnetization curves of oriented single crystals at 20 K. c) ZFC (red) and FC (orange) χ(T) plots. The arrows show T_F, Tc and T_{JT} with the respective crystal symmetries. d-e) XRD patterns of obtained powders using d) $BaCO_3$ and e) $Ba(NO_3)_2$ precursors. Strong preferred orientations effects are observed in the second one. f-g) Rhombic crystals products with white $BaCoO_3$ phase before filtering vs. h-i) plate-like crystals within a homogeneous sample before filtering.

3. Experimental

3.1 Synthesis

The preparation of polycrystalline and single crystals of BFPO was explained elsewhere using a hydrothermal method with hydrazine as a reducing agent to constrain a single Fe^{2+} valence and $BaCO_3$ as the barium source [8,13–15]. However, the obtained single crystals are rhombohedral in form, which does not allow for an easy access to the (001) planes, in which

the honeycomb layers are developed. $BaFe_2(PO_4)_2$ platelet-like single crystals growing along the (001) plane, were obtained in the present work, hydrothermally using a stoichiometric mixture of $Ba(NO_3)_2$, $FeCl_2 \cdot 4H_2O$ dissolved in H_3PO_4 (2 mL, 65%), and 2–3 drops of hydrazine placed in a 23 mL Teflon lined autoclave filled to 2/3 with deionized water. The reactor was directly placed in the oven heated at 220 °C for 24 h and quenched to room temperature. The crystals were recovered by filtration and washed with water and ethanol in an ultrasonic bath. See the XRD patterns of the resulting batches in Figure 1d-e. The superior solubility of the nitrate compared to the carbonate precursor and their relative complexation constants are likely the main ingredients for this crystal habit changes. We note that before filtration that white grains of $BaCO_3$ are present in the reaction products, contrarily to the homogeneous color found using nitrates, see Figure 1 f,g,h,i. Despite the misleading colors of the distinct crystals shown in the Figure 1 due to their light reflectivity, they are all yellow under the optical microscope with a more greenish color tone for the thicker ones. In order to be certain that no concentration of Fe^{3+} defects mentioned earlier was present, special care was taken in both single crystals and powders and all samples have been refined to the same lattice parameters within +/-0.2% along *a* and +/- 0.01% along *c*. These homogeneous values emphasize the efficient role of the hydrazine reducing agent to stabilize Fe^{2+} species, while only Fe^{3+} traces are expected.

The XRD patterns show strong preferred orientation effects for the platelet ones. The handling of platelets with the easy magnetic axis perpendicular to the crystal main faces is mandatory, for the easy crystal alignment and informative magnetic force microscopy experiments. The crystal growth mechanism is rather complex and out of the focus of this work. In brief, in the prime stage, we observed the precipitation of $BaH(PO_4)$ + $BaFe_3(PO_4)_3$ which are progressively transformed in favor of the final $BaFe_2(PO_4)_2$ after 24 hours of reaction. A longer reaction time favors the reverse reaction towards a biphasic mixture.

3.2 Magnetic Measurements

Isotropic properties were measured on polycrystalline powders, whereas anisotropic properties used oriented single crystals. Single crystals were dispersed in epoxy resin and cured under magnetic field at room temperature. Rotation of the cured epoxy allow to change the orientation of the crystals with respect to the applied magnetic field.

AC magnetic susceptibility measurements on powder samples were obtained on a Quantum design MPMS-Squid magnetometer with excitation frequencies between 1 and 1000 Hz, in the 2-85 K temperature range, H_{AC} = 5 Oe. The dynamics were analyzed using a Cole-Cole model, details about the fitting procedures are reported elsewhere [17].

DC measurements up to 9 T were collected on a VSM-PPMS while a MPMS-Squid magnetometer was used for measurements up to 14 T. Typical experiments were performed using zero field cooled (ZFC) and field cooled (FC) procedures in the 1.8-400 K temperature range under a 0.1 T field.

The dependency of the magnetization (*M*) to the applied field (*H*) was studied using the Arrott–Noakes equation [18]. The fitted parameters, β and γ correspond to the 2D-Ising model [17].

Neutron inelastic data (not presented here) were analyzed with the mean field and spin wave expansion carried out with the Spinwave software developed at LLB [19]. Assuming the exchange coupling J = 14 K deduced from the exact solution of the Honeycomb S = 2 case, we determined from the comparison between calculation and measurement an Ising anisotropy parameter D_z = 54 K for the Fe sites, equivalent to K = 0.67 KÅ^{-3}.

3.3 Magnetic Force Microscopy (MFM)

Measurements were performed using an attocube attoDRY1000 closed-cycle cryogenic microscope in the temperature 4-50 K and up to 9 T. CoCr-coated silicon probes, magnetized at T = 60 K and H = 2000 Oe, with a resonance frequency of 157 kHz, a spring constant of 5 Nm^{-1}, and coercivity of ≈ 1500 Oe (MESP-RC, Bruker) were used detailed description of the experimental setup can be found elsewhere [20–24].

The crystals were hand placed on a titanium coated silicon holder with the [001] direction normal to the plane of the holder. All MFM images were taken in a buffer gas cooling of helium at 0.5 mbar , with a temperature stability of ± 0.3 mK.

Hereinafter, MFM imaging of the domain structure at $T < T$(FM) was performed in a lift mode. In this mode, the tip is lifted by 50 nm above the surface, thus avoiding the distortion of the magnetic structure maps due to magnetic interaction with the MFM tip.

4. Results and Discussion

4.1 Magnetic Domains and their pinning:

We recently detected on fixed single crystals and powders, pronounced spin dynamic changes on cooling due to the freezing of magnetic domains below T_F = 15 K where a soft → super-hard magnet transition occurs [17]. Below the nearly frequency-independent peak at T_C detected on AC-χ''(T), a dynamical contribution is observed as a rounded shoulder below 40 K shifted to higher temperature on increasing the AC-frequency, see Figure 2a. The distribution of susceptibility $\Delta\chi_{AC}$ between high f and static values was priory analyzed by a Debye model with a barrier distribution [25] and shows a linear regime between T_C and 23 K, then another transitory linear regime down to T_F = 15 K. Below T_F, a complete freezing of the spin dynamics is evidenced by χ' and χ'' = 0 [17]. This transition is responsible of the progressive opening of M(H) hysteresis with unprecedent coercive and remanent characteristics. It was measured on single crystals preliminary embedded in drying epoxy and aligned in an applied field of 9 T at 250 K, see Figure 2b and 2c. Between T_C and ~23 K, the coercivity H_c is very weak (~0.1 T) and almost temperature-independent. The *S*-like shape with easy reversal of the spins is typical of 2D-FM systems. Below 23 K, the coercive field slightly increases, which corresponds well to the so-called "transitory regime" aforementioned. It reaches 0.8 T at T_F = 15 K, where H_c evolves in a linear regime with the temperature. At 6 K, we measured H_c = 11.3 T, below which the M(H) cycles are not symmetrical anymore, due to irreversible depinning of the magnetic-domains limited by our maximal applied field of 14T. Below this temperature (shown in grey in Figure 2b,c) H_c is under evaluate and deviates from the linear law which at 0 K extrapolates to H_c = 19.6 T. Such a giant value exceeds the extrapolated at 0 K for $LuFe_2O_4$ (~9 T), in which similar freezing process was evidenced [7]. At 5 K, we calculated a $B.H_{max}$ Figure of merit (*i.e.*, energy product) of 6.5 MG.Oe typical of hard magnets, see Figure 2d. In our case, the detrimental parameter B (=4πM+ H) is limited by the volumetric magnetization M due to the important contribution of the non-magnetic spacers. It is superior to the ones reported for oxide permanent magnets, however this occurs at low temperature but with a rarely observed rapid passage from a soft to super-hard magnet.

Concerning the domain-walls in BFPO, the quantitative data were abundantly discussed in [17]. Summarizing those results, their width can be estimated from the numerical knowledge of *i)* the ferromagnetic J exchange value (~14 K), leading to the exchange stiffness of ~46.14 $KÅ^{-1}$ (a kind of density of magnetic exchange with respect to the 1D honeycomb lattice-type) and *ii)* the magnetic anisotropy estimated to the giant value K = 0.67 $KÅ^{-3}$ deduced from the modelization of our inelastic data spectra using a spin-wave approximation over a honeycomb 2D-sub-unit. It finally leads to the narrow wall thickness $\delta_{DW} = \pi\sqrt{(A/K)} = \approx$ 26 Å,

i.e. 10 Fe-Fe contacts, far below the 400 Å generally estimated for metal Fe. The energy cost of the wall is given by $E_{DW}/k_B = 4\sqrt{(AK)} = 22.2$ K Å^{-2} [26].

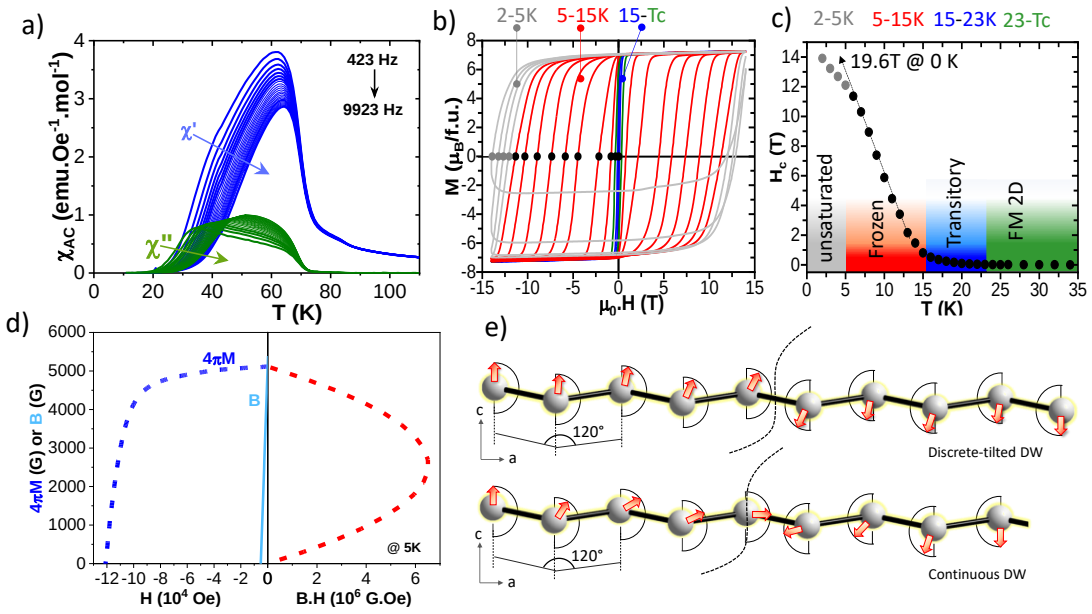

Figure 2: a) Real and imaginary parts of χ_{ac} (T) measured on BFPO single crystals. b) M(H) plots on cooling at different temperatures below T_c on oriented single crystals. c) The deduced coercitive fields H_c versus temperature. d) B.Hmax energy product graphically calculated from the data at T=5K (B is the limiting factor). e) top: narrow magnetic domain walls with small tilts between the spins. bottom: continuous Bloch-like wall, shortened for comparison. The zigzag dotted-line delimits the center of the DWs.

Furthermore, the linear evolution of H_c versus T suggests a so-called "weak pinning regime" ($H_c \propto A+BT$) rather than a "strong pinning regime" ($H_c^{½} \propto A–BT^{2/3}$). Conceptually, these two models developed by Gaunt [27] differ in that the strong pinning demagnetization is considered to be the breaking of the wall from a single spin-defect, while for the weak pinning, the walls break away from many pins simultaneously in a cooperative manner. From the exact parametrization of the weak-pinning equation $H_c/H_0 = 1–(25\ kT)/(E_{DW}\cdot b^2)$, with b is 1/4th of the domain width and $H_0 = 19.6$ T and using the E_{DW} value given above, we find $\delta_{DW} = 16$ Å in close agreement with the value of 26 Å suggested above. Finally, our magnetic domains materialize with very narrow walls, due to predominant anisotropy over the J exchange for BFPO and fixed by multiple pin centers with respect to a weak pinning model. It is probable that the propagation of the domains between the stacked individual layers is performed by dipole-dipole interactions across the crystal z-axis. We recall that in BFPO, the 2D-Ising nature was validated by the calculation of nearly-zero inter layer exchanges [8].

4.2 Domain imaging by MFM

The domains as observed by MFM appeared immediately below T_C. Figure 3a shows their stripe-like structure while the crystal was cooled down to 4.4 K in a residual-field of the solenoid, with a non-perfectly demagnetized cantilever probe. On this figure, blue and red areas correspond to up and down moments, respectively. Increasing the field to 0.5 T and heating the sample above T_F leads to an almost complete spin-reversal, besides residual row like defects, see Figure 3b. This picture strongly differs from what expected for a random distribution of lattice defects. After cooling the sample in perfectly demagnetized conditions, so-called zero-field cooled (ZFC, for both the solenoid and the cantilever), a very different image of the same scanned area is obtained, see Figure 3c where we obtain a much more labyrinthic domain

structure which does not conserve common domain wall fragments in comparison to Figure 3a. These results validate the participation of multiple pinning-centers, which may depend on the sample-history, different from the lattice or chemical defects picture. Moreover, firing our single crystals at 500°C in pure flowing H_2 in order to remove all possible '*Fe^{3+}/vacancy* 'defect pairs (see *section 2*) led to similar results. This refutes any strong influence of chemical/lattice defects in the pinning process. It does show a good agreement with the "intrinsic" pinning scheme stabilized by narrow domains,[28] which are naturally developed even in ideal perfect crystals. Here, the tilting angles along the walls are small discrete values with moments nearly parallel to the *c*-axis, see Figure 2e-top. The centers of the domain walls pass in between two next Fe–Fe neighbors, otherwise costing a large energy gap, if the central atom is assigned to an *in-plane* spin. Using the results of [28], after normalization of the exchange energy per volume leading to J_V = 0.17 K/Å^{-3}, we calculate K/J_V ~ 3.9. For such value, the energy difference ΔE between a continuous Bloch-like domain (see Figure 2e-bottom) and a sharp-one is estimated to $\Delta E = a \cdot K$ = 1.88 K.Å^{-2}, where a is the Fe–Fe distance of 2.8 Å in the walls. In such case, the coercive force H_c is given by: $H_c = (\pi \cdot \Delta E)/(2a \cdot I_s)$ with I_s the saturated value at 0 K, i.e. 0.05 μ_B/Å^3 in BFPO, counting six S = 5μ_B per unit cell, from the magnetic structure refinement [8,13] and since one μ_B is 0.672 K/T, we obtained $H_{c,\,@\,0K}$ = 25 T in line with the extrapolation of our experimental data toward H_c = 19.6 T.

Finally, the model developed for intrinsic pinning in absence of chemical defects predicts well our data, and one should consider the demagnetization process as the wall motion induced by a collective reversal of discrete spins in the walls. Figure 3d shows the robustness of our walls, as the domain structure remains unchanged below T_F, increasing the applied field along the easy-axis up to 6 T.

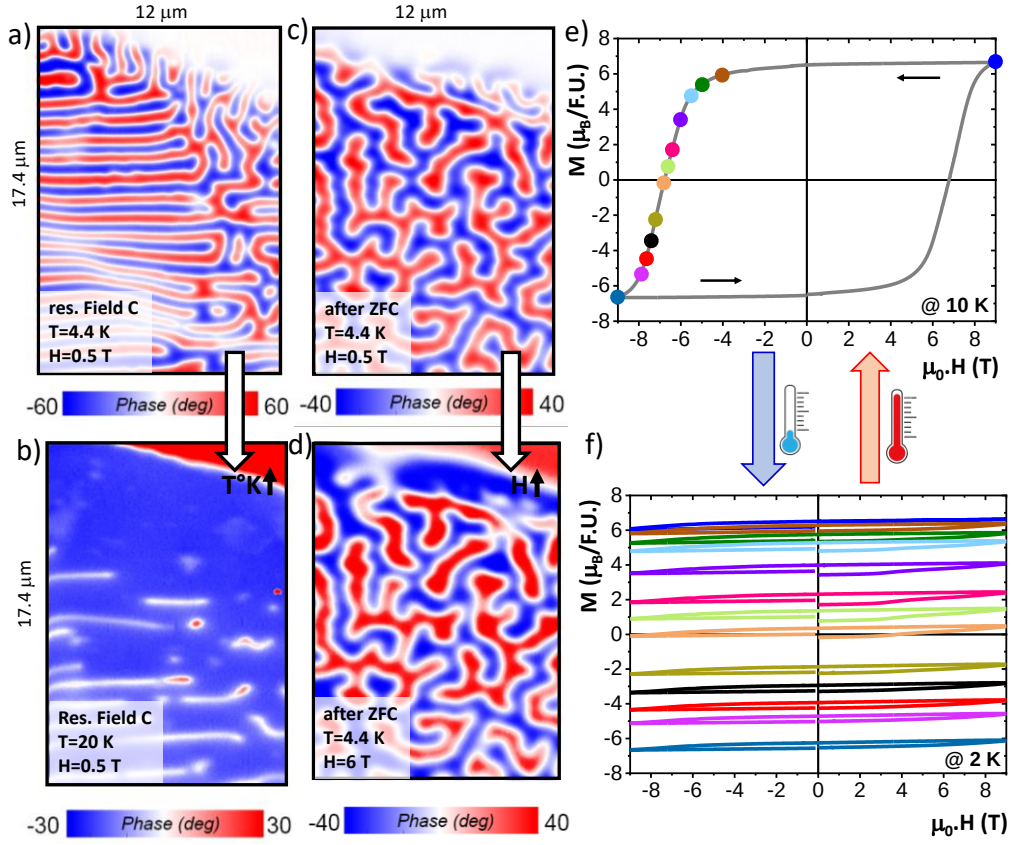

Figure 3: a-b) striped DW structure in BFPO after cooling in a residual magnetic field before and spin reversal after heating from 4.4 to 20 K, H=0.5 T. c-d) labyrinthic DW structure in BFPO (same area that for a)) after zero field cooling. It remains unchanged under a field of 6T below T_F. e) M(H) Hysteresis loop at T = 10 K. The

colored points correspond to different magnetization states, chosen to demonstrate the concept of a BFPO magnetic memory. f) M(H) Hysteresis loop quenched at T = 2 K from the various precedent points.. The magnetization remains essentially flat, whatever the field (coercive force > 15 T), indicating unswitchable magnetic states at T = 2 K.

It was already intensively detailed in ref. [17] that the passage on cooling from open M(H) hysteretic cycles at 10 K, limiting the external field between -9 and 9T (Figure 3e), to perfectly frozen states at 2K in the same range of field (Figure 3f), allows for the imprint of any bulk magnetization, just tuning on the temperature. At the nanometric level, only two domains, one "up" and one "down" growing at each other expenses should allow to pin any magnetization between $-M_{sat.}$ and $+M_{sat}$. This is further discussed below.

4.3 Heat capacity

The heat capacity of the rhombohedral γ-BFPO polytype concerned here, and those of its high temperature form α-BFPO [29] are shown in Figure 4. The later orders antiferromagnetically below $T_N \approx 15$ K, with the appearance of a significant ferromagnetic contribution. It is assigned to a canted spin structure due to a corner sharing $Fe^{2+}O_5$ square-pyramidal structure, similarly to α-BCoPO (T_N = 17 K) [30]. Using single crystals of γ-BFPO both the Jahn-Teller at T_{JT} =140 K and the Curie transitions are sharply marked on Cp(T) curve and amplified on the Cp/T(T) plot, see Figures 4a and 4b. The effect of an applied magnetic field flattens the λ-anomaly at *Tc* and shifts it toward higher temperature. This is in line with ferromagnetic correlations above *Tc*, enhanced by an external field. However, this effect is less drastic at T_{JT} which allows to refute the influence of magnetic exchanges in the first event of the re-entrant structural transition discussed above.

Using a polycrystalline pelletized sample, these effects are appreciably smeared, this allows for a more-standard treatment in a sufficiently large thermal domain. For both γ and α polycrystalline compounds the lattice-phonon contribution was fitted using the sum of a Debye integral and two Einstein terms well suited to describe the heat capacities of minerals [31] :

$$C_{latt} = 9R\, C_D(T/\theta_D)^3 \int_0^{\theta_{Di}/T} \frac{x^4\, e^x}{(e^x-1)^2}\, d_x + \sum_{i=1}^{2} C_{Ei}\, 3R\, (\theta_{Ei}/T).(\exp(\theta_{Ei}/T)).(\exp(\theta_{Ei}/T)-1)^{-2}$$

Here $C_D + C_{E1} + C_{E2}$ is constrained to 13, the number of atoms per formula unit. The magnetic contribution C_{magn} was deduced by subtraction of C_{latt} (see Figures 4c and 4e) and transformed to the corresponding magnetic entropy by integration of C_{magn}/T over the temperature, see Figures 4d and 4f.

For γ-BFPO, the magnetic contribution is significant until ~120 K, in good agreement with the strong in-plane 2D-FM correlations above T_C, already reported [13]. However, a slight deviation occurs at higher temperatures due to the Jahn-Teller induced structural transition. In comparison, α-BFPO C_{magn} becomes neglectable above ~50 K. Unexpectedly, low temperature γ-BFPO C_{magn}/T shows a significant contribution below *Tc*, which corresponds to the zero-field low frequency $\chi'(T)$ maximum. This highlights the addition to the heat capacity from the domain-spin dynamics. C_{magn}/T shows a bump at T_F at which the released entropy increases more abruptly, in line with the defreezing of robust magnetic domains. There are only rare reports on the influence of the ferromagnetic magnetic domains on the heat capacity, for instance in the ferromagnet $CdCr_2Se_4$, the heat capacity approaches the theoretical curve only above ~0.5 T [32]. It was then proposed that the zero-field magnon heat capacity is diminished by the presence of magnetic domain walls. Thus, the expected field dependence is only restored when the sample turns into a single domain state thanks to the applied magnetic field. Although the methodology is different, our results are somehow compatible since the entropy release at T_C is much lower due to the strong contribution down to T_F. In both samples the expected magnetic entropy release 2R.ln(2S+1) = 26.85 J/ K.mol is approximately reached, though in a more narrow thermal domain for α-BFPO.

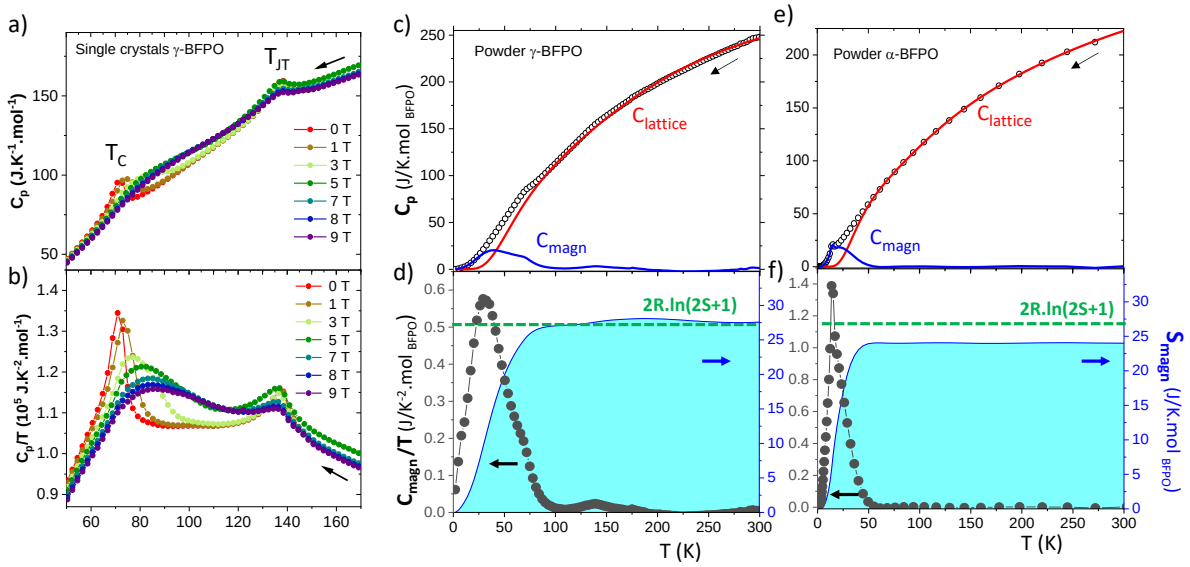

Fig. 4: a-b) Cp(T) and Cp/T(T) curves for single crystals of γ-BFPO at various fields. c) Lattice and magnetic contributions to Cp(T) for polycrystalline γ-BFPO. d) C_{magn}/T and the magnetic entropy after integration to the temperature. e-f) Same data for polycrystalline α-BFPO.

5. Conclusion

In conclusion, this work describes the micromagnetic properties of BFPO for which the competition between exchange and anisotropy parameters enforce the freezing of spins below $T_F \approx 15$ K. While this phenomenon has been reported in a handful of inorganic materials with high uniaxial magneto-crystalline anisotropy, BFPO is remarkable due to the spin flipping in the magnetic very narrow domain walls (≈16 Å) responsible for the intrinsic and robust pinning of these below T_F. This aspect allows for reproducible results, independent of the sample quality and crystallinity. Magnetic force microscopy images of the domains as a function of field and temperature validate the domain pinning as the driving force of the giant-coercivity. The robust freezing of "spin up" and "spin down" domains in BFPO and their motion above T_F offers several potentialities. The most striking one concerns the possible imprint and locking of any magnetization in the saturation limits on a single crystal, due to the giant coercivity in the frozen state. This original property allows temperature-field cycling between an open hysteresis (just below T_F, *e.g.* 10 K) and a temperature assorted with giant coercivity, *e.g.* 2 K. We imprinted at 10 K several magnetic states at various fields, and pinned them between -9 and 9 T at 2 K, after cooling. This indicates the possibility to imprint multiple magnetization states (12 states in Figure 3f). Hence, our system allows for a new paradigm to be realized with multi-state memory by freezing of magnetic domains toward the realization of a nonvolatile system for high density storage.

6. Acknowledgment

The Chevreul Institute (FR 2638), Region Hauts-de-France, and FEDER are acknowledged for funding the X-ray diffractometers and the PPMS magnetometer. Low-temperature MFM studies were supported by the RSF grant No.23-72-30004 (https://rscf.ru/project/23-72-30004/). Sample preparation for MFM studies was supported by the Ministry of Science and

Higher Education of the Russian Federation (No. FSMG-2023-0014). ILL and Lille University are thanked for the J.W. PhD thesis financial support.

[1] R.M. Bozorth, Magnetic domain patterns, J. Phys. Radium. 12 (1951) 308–321.
[2] S.S.P. Parkin, M. Hayashi, L. Thomas, Magnetic Domain-Wall Racetrack Memory, Science. 320 (2008) 190–194. https://doi.org/10.1126/science.1145799.
[3] D.A. Allwood, G. Xiong, C.C. Faulkner, D. Atkinson, D. Petit, R.P. Cowburn, Magnetic Domain-Wall Logic, Science. 309 (2005) 1688–1692. https://doi.org/10.1126/science.1108813.
[4] A. Hoffmann, S.D. Bader, Opportunities at the Frontiers of Spintronics, Phys. Rev. Appl. 4 (2015) 047001. https://doi.org/10.1103/PhysRevApplied.4.047001.
[5] G. Vértesy, I. Tomás, Z. Vértesy, On the temperature dependence of domain wall pinning field in soft, uniaxial magnetic materials, J. Phys. Appl. Phys. 35 (2002) 625. https://doi.org/10.1088/0022-3727/35/7/310.
[6] R. Das, V. Kalappattil, M.-H. Phan, H. Srikanth, Magnetic anomalies associated with domain wall freezing and coupled electron hopping in magnetite nanorods, J. Magn. Magn. Mater. 522 (2021) 167564. https://doi.org/10.1016/j.jmmm.2020.167564.
[7] W. Wu, V. Kiryukhin, H.-J. Noh, K.-T. Ko, J.-H. Park, W. Ratcliff, P.A. Sharma, N. Harrison, Y.J. Choi, Y. Horibe, S. Lee, S. Park, H.T. Yi, C.L. Zhang, S.-W. Cheong, Formation of Pancakelike Ising Domains and Giant Magnetic Coercivity in Ferrimagnetic $LuFe_2O_4$, Phys. Rev. Lett. 101 (2008) 137203. https://doi.org/10.1103/PhysRevLett.101.137203.
[8] H. Kabbour, R. David, A. Pautrat, H.-J. Koo, M.-H. Whangbo, G. André, O. Mentré, A Genuine Two-Dimensional Ising Ferromagnet with Magnetically Driven Re-entrant Transition, Angew. Chem. Int. Ed. 51 (2012) 11745–11749. https://doi.org/10.1002/anie.201205843.
[9] J. Fischbacher, A. Kovacs, H. Oezelt, M. Gusenbauer, T. Schrefl, L. Exl, D. Givord, N.M. Dempsey, G. Zimanyi, M. Winklhofer, G. Hrkac, R. Chantrell, N. Sakuma, M. Yano, A. Kato, T. Shoji, A. Manabe, On the limits of coercivity in permanent magnets, Appl. Phys. Lett. 111 (2017) 072404. https://doi.org/10.1063/1.4999315.
[10] L.J. de Jongh, Magnetic Properties of Layered Transition Metal Compounds, Springer Science & Business Media, 1990.
[11] Y. Liu, L. Wu, X. Tong, J. Li, J. Tao, Y. Zhu, C. Petrovic, Thickness-dependent magnetic order in CrI_3 single crystals, Sci. Rep. 9 (2019) 13599. https://doi.org/10.1038/s41598-019-50000-x.
[12] K. Prokeš, V. Sechovský, A. Gukasov, A.V. Andreev, H. Nakotte, Direct measurement of the magnetic anisotropy in UCoGa using polarized neutrons, Phys. B Condens. Matter. 276–278 (2000) 564–565. https://doi.org/10.1016/S0921-4526(99)01788-3.
[13] R. David, A. Pautrat, D. Filimonov, H. Kabbour, H. Vezin, M.-H. Whangbo, O. Mentré, Across the Structural Re-Entrant Transition in $BaFe_2(PO_4)_2$: Influence of the Two-Dimensional Ferromagnetism, J. Am. Chem. Soc. 135 (2013) 13023–13029. https://doi.org/10.1021/ja404697b.
[14] R. David, H. Kabbour, D. Filimonov, M. Huvé, A. Pautrat, O. Mentré, Reversible Topochemical Exsolution of Iron in $BaFe^{2+}{}_2(PO_4)_2$, Angew. Chem. Int. Ed. 53 (2014) 13365–13370. https://doi.org/10.1002/anie.201404476.
[15] I.B. Alcover, R. David, S. Daviero-Minaud, D. Filimonov, M. Huvé, P. Roussel, H. Kabbour, O. Mentré, Reversible Exsolution of Nanometric Fe_2O_3 Particles in $BaFe_{2-x}(PO_4)_2$ ($0 \leq x \leq 2/3$): The Logic of Vacancy Ordering in Novel Metal-Depleted Two-Dimensional

Lattices, Cryst. Growth Des. 15 (2015) 4237–4247. https://doi.org/10.1021/acs.cgd.5b00525.
[16] I. Blazquez Alcover, S. Daviero-Minaud, R. David, D. Filimonov, M. Huvé, J.P. Attfield, H. Kabbour, O. Mentré, Selective Metal Exsolution in $BaFe_{2-y}M_y(PO_4)_2$ (M = Co^{2+}, Ni^{2+}) Solid Solutions, Inorg. Chem. 54 (2015) 8733–8743. https://doi.org/10.1021/acs.inorgchem.5b01360.
[17] O. Mentré, B. Leclercq, A.M. Arevalo-Lopez, A. Pautrat, S. Petit, C. Minaud, S. Daviero-Minaud, R.A. Hovhannisyan, V.S. Stolyarov, Multivalued Memory via Freezing of Super-Hard Magnetic Domains in a Quasi 2D-Magnet, Small Methods. 7 (2023) 2300491. https://doi.org/10.1002/smtd.202300491.
[18] A. Arrott, J.E. Noakes, Approximate Equation of State For Nickel Near its Critical Temperature, Phys. Rev. Lett. 19 (1967) 786–789. https://doi.org/10.1103/PhysRevLett.19.786.
[19] S. Petit, Spinwave, (n.d.). https://www. llb.cea.fr/logicielsllb/SpinWave/SW.html.
[20] V.S. Stolyarov, I.S. Veshchunov, S.Yu. Grebenchuk, D.S. Baranov, I.A. Golovchanskiy, A.G. Shishkin, N. Zhou, Z. Shi, X. Xu, S. Pyon, Y. Sun, W. Jiao, G.-H. Cao, L.Ya. Vinnikov, A.A. Golubov, T. Tamegai, A.I. Buzdin, D. Roditchev, Domain Meissner state and spontaneous vortex-antivortex generation in the ferromagnetic superconductor $EuFe_2(As_{0.79}P_{0.21})_2$, Sci. Adv. 4 (2018) eaat1061. https://doi.org/10.1126/sciadv.aat1061.
[21] S.Yu. Grebenchuk, Zh.A. Devizorova, I.A. Golovchanskiy, I.V. Shchetinin, G.-H. Cao, A.I. Buzdin, D. Roditchev, V.S. Stolyarov, Crossover from ferromagnetic superconductor to superconducting ferromagnet in P-doped $EuFe_2(As_{1-x}P_x)_2$, Phys. Rev. B. 102 (2020) 144501. https://doi.org/10.1103/PhysRevB.102.144501.
[22] V.V. Dremov, S.Y. Grebenchuk, A.G. Shishkin, D.S. Baranov, R.A. Hovhannisyan, O.V. Skryabina, N. Lebedev, I.A. Golovchanskiy, V.I. Chichkov, C. Brun, T. Cren, V.M. Krasnov, A.A. Golubov, D. Roditchev, V.S. Stolyarov, Local Josephson vortex generation and manipulation with a Magnetic Force Microscope, Nat. Commun. 10 (2019) 4009. https://doi.org/10.1038/s41467-019-11924-0.
[23] V.S. Stolyarov, V. Ruzhitskiy, R.A. Hovhannisyan, S. Grebenchuk, A.G. Shishkin, O.V. Skryabina, I.A. Golovchanskiy, A.A. Golubov, N.V. Klenov, I.I. Soloviev, M.Yu. Kupriyanov, A. Andriyash, D. Roditchev, Revealing Josephson Vortex Dynamics in Proximity Junctions below Critical Current, Nano Lett. 22 (2022) 5715–5722. https://doi.org/10.1021/acs.nanolett.2c00647.
[24] S.Yu. Grebenchuk, R.A. Hovhannisyan, A.G. Shishkin, V.V. Dremov, V.S. Stolyarov, Magnetic Force Microscopy for Diagnosis of Complex Superconducting Circuits, Phys. Rev. Appl. 18 (2022) 054035. https://doi.org/10.1103/PhysRevApplied.18.054035.
[25] H.B.G. Casimir, F.K. du Pré, Note on the thermodynamic interpretation of paramagnetic relaxation phenomena, Physica. 5 (1938) 507–511. https://doi.org/10.1016/S0031-8914(38)80164-6.
[26] D. Jiles, Introduction to Magnetism and Magnetic Materials, 1998.
[27] P. Gaunt, Ferromagnetic domain wall pinning by a random array of inhomogeneities, Philos. Mag. B. 48 (1983) 261–276. https://doi.org/10.1080/13642818308228288.
[28] J. van den Broek, H. Zijlstra, Calculation of intrinsic coercivity of magnetic domain walls in perfect crystals, IEEE Trans. Magn. 7 (1971) 226–230. https://doi.org/10.1109/TMAG.1971.1067036.
[29] B. Leclercq, H. Kabbour, A. Arevalo-Lopez, M. Huvé, S. Daviero-Minaud, C. Minaud, I.B. Alcover, O. Mentré, Polymorphs, phase transitions and stability in $BaM_2(PO_4)_2$ M = Mn, Fe, Co systems, Inorg. Chem. Front. 7 (2020) 239–246. https://doi.org/10.1039/C9QI00934E.

[30] R. David, H. Kabbour, A. Pautrat, O. Mentré, Puzzling Polymorphism of Layered $Ba(CoPO_4)_2$, Inorg. Chem. 52 (2013) 8732–8737. https://doi.org/10.1021/ic4009027.
[31] E. Gamsjägger, M. Wiessner, Low temperature heat capacities and thermodynamics functions described by Debye-Einstein integrals, Montasch Chem. 149 (2018), 357-368. https://doi.org/10.1007/s00706-017-2117-3
[32] K-H. Ahn , Z. Jirak , K. Knízek , P. Levinský , M. Soroka , L. Benes , J. Zich , J. Navratil, J. Hejtmanek, Heat capacity and thermal conductivity of $CdCr2Se_4$ ferromagnet: Magnetic field dependence, experiment and calculations, Journal of Physics and Chemistry of Solids 174 (2023) 111139. https://doi.org/10.1016/j.jpcs.2022.111139